Catalysis Science & Technology

ROYAL SOCIETY OF CHEMISTRY

PAPER

View Article Online
View Journal | View Issue

Check for updates

Cite this: *Catal. Sci. Technol.*, 2026, **16**, 2971

A high-throughput reactor array applied to the parameter exploration of copper-exchanged zeolites for dilute methane oxidation

Elijah E. Martin, *[a] William J. Sawyer, [ab] Karl S. Westendorff, [c] A. John Hart [b] and Desirée L. Plata *[a]

Received 12th January 2026,
Accepted 20th March 2026

DOI: 10.1039/d6cy00033a

rsc.li/catalysis

Methane abatement through thermocatalysis could be a powerful tool to reduce sub-flammable methane emissions. Copper-doped zeolites are cost-effective, earth-abundant alternatives to platinum group metal catalysts that have demonstrated oxidation of dilute methane (*i.e.*, less than 1% CH_4). Optimization of these copper catalysts necessitates high-throughput experimentation to efficiently explore the complex parameter space governing catalyst activity and catalyst kinetics. Here, we designed, built, and demonstrated the use of a high-throughput reactor for heterogeneous catalysis (catalytic array for screening and high-throughput discovery (CASHD)). CASHD consists of eight reactors with individual temperature, flow, and effluent valve control. The system was used to screen 16 catalysts consisting of different zeolite frameworks (BEA, FER, MFI, and MOR) and copper loadings (1.8–5.0 wt%). The best performing zeolite catalyst tested, as measured by a light-off curve, was 4.3 wt% Cu MFI with a T_{50} of 366 °C. The catalysts' kinetics were subsequently evaluated through an Arrhenius experiment. BEA catalysts, generally had higher activation energies, averaging to 119 ± 16 kJ mol^{-1}, than FER, MFI, and MOR which had average activation energies of 87 ± 4, 85 ± 7, and 94 ± 7 kJ mol^{-1}, respectively. Two *in situ* characterization techniques complemented these kinetic analyses: diffuse reflectance ultraviolet-visible spectroscopy to probe the catalyst surface and isotopic-abundance analysis to quantify the effluent gas. Such high-throughput experimentation as demonstrated on the CASHD system will enable better integration of computationally enhanced materials discovery with experimental validation, accelerating catalyst discovery for low-temperature methane abatement catalysts.

Introduction

Methane's high global warming potential and short atmospheric lifetime make it a powerful lever for mitigating global temperature rise.[1] Methane emission reduction has garnered attention internationally as a tool to help meet the Paris Agreement's 2 °C target, where 57% reductions in anthropogenic emissions by 2030 may translate to 0.5 °C savings in climate forcing.[2,3] Converting methane emissions to carbon dioxide yields a climate benefit by reducing the net radiative forcing.[1,4] Unfortunately, the majority of methane emissions are dilute (*i.e.*, below the lower flammability limit of 5 v/v%), with few technologically viable options for their reduction.[4] Thermocatalysis has been demonstrated to be useful in abating these sub-flammable methane emissions; however, widespread adoption has been limited due the catalyst's high cost, poor resistance to chemical interferents (*e.g.*, humidity and sulfur-containing gases), and moderate energy requirements.[4–6] Copper zeolites offer an earth-abundant, cost-effective alternative to the widely used platinum group metal catalysts.[7–11]

Copper zeolites have been extensively studied in partial methane oxidation (PMO) to methanol,[12–15] but assessment of these materials for complete oxidation is underexplored.[7,11] For PMO, high methane (*i.e.*, greater than 18 v/v%) and oxygen availability control (*i.e.*, low oxygen concentrations continuously or high concentrations run as a pretreatment step before methane introduction help prevent over-oxidation of methane to carbon dioxide.[15–20] While such requirements make PMO impractical for dilute methane emissions management, there are transferable materials insights that can guide research into complete methane oxidation. In the PMO reaction, there is wide agreement that the most reactive active site is a copper dimer, whose copper atoms cycle between an oxidation state of +1 and +2 during

[a] *Department of Civil and Environmental Engineering, Massachusetts Institute of Technology, Cambridge, MA, 02139, USA. E-mail: elijahma@mit.edu, dplata@mit.edu*
[b] *Department of Mechanical Engineering, Massachusetts Institute of Technology, Cambridge, MA, 02139, USA*
[c] *Department of Chemical Engineering, Massachusetts Institute of Technology, Cambridge, MA, 02139, USA*

reaction and activation, respectively.[17,21–24] For methane combustion over copper zeolites, there is little consensus on the active site. M'Ramadj *et al.* speculated that surface CuO nanoparticles are responsible[11] but Brenneis *et al.*, have shown combustion activity in the absence of the CuO(111) X-ray diffraction line.[7] Regardless, to our knowledge only three copper zeolite catalysts at very limited condition sets have been tested.[7,11] More catalysts need to be tested to better understand the structure–activity relationships governing these materials and to optimize the catalyst's performance. To fully elucidate catalyst performance, systematic variation of copper loading, zeolite framework, pretreatment conditions, and reaction conditions is needed. The urgency of methane mitigation necessitates the use of high-throughput experimentation (*i.e.*, increased experimental productivity due to efficiency gains in space or time) to explore this complex parameter space.

High-throughput experimentation will become increasingly necessary to develop robust, intercomparable datasets (*e.g.*, dataset uniformity will be enhanced when experiments are conducted on a single automated system) to inform artificial intelligence-based materials discovery and has been of growing interest in recent years. Publications with the words "high-throughput experimentation" have increased roughly 5-fold in the last 20 years resulting in 1470 total publications (2004–2024; Table S1 and Fig. S1). However, the total number of publications that use high-throughput reactors for catalysis is only 278 (5 times lower) and the publication rate has remained relatively constant. Existing high-throughput reactors that are most closely aligned with methane combustion catalysis fall short in their analytical instrument integration, temperature tuneability, and their flexibility to conduct both screening and kinetic studies.[25,26] Additionally, most published high-throughput reactor work has often not included characterization of uncertainty, sacrificed throughput with triplicate experiments, or used the generation of a large dataset as justification for the omission of uncertainty quantification.[25–28] Note that high-throughput reactors can be purchased from commercial vendors,[28–31] when the desired reaction suits the available design. However, due to the highly specific nature of many reactions and especially those in heterogeneous catalysis, many such systems are not readily adaptable to other chemistries. This can result from variation in reactant and product phases, associated *in situ* diagnostics or online characterization, and necessary process parameter ranges, ultimately requiring tailored reactors.[27,28,31–33]

Here, we designed and built a high-throughput reactor for solid–gas heterogenous catalysis tailored to, but not limited to, methane oxidation catalysis. We then demonstrated a new workflow to quantify reactor variability in CASHD's primary mode of operation, screening, to evaluate copper zeolite catalysts. These catalysts were then further characterized using CASHD's secondary mode of operation, kinetic testing. Finally, we integrated *in situ* high-throughput diagnostic characterization methods for the gases and solids in combination with reaction data to gain better insight into the reaction mechanism and active site type.

Methods

Reactor design

A system was developed and termed the catalytic array for screening and high-throughput discovery (CASHD). CASHD is a manifold of eight vertical tube furnaces that have independent heating and gas flow, enabling testing of up to eight catalysts simultaneously under decoupled conditions (Fig. 1). Each furnace consisted of a heating element and 50 mm of radial insulation (Fig. S2). A custom-machined aluminum tube with a coil heater (Tempco Mightyband) wrapped around it was used as the heating element, resulting in a heated zone length of 150 mm. A quartz reaction tube was placed in the center of the furnace. The quartz tube [20 mm × 500 mm (ID × length)] was modified with a frit (placed halfway down the tube; Technical Glass Products) to hold the catalyst.

Flow control. Air (ultra-zero air, Linde AI 0.0UZ-T), and methane (99.97% purity, Linde ME 3.7UH-T) flows are specified with mass flow controllers (0–5 SLPM with accuracy ±0.6% of reading or ±0.1% of full scale, whichever is greater and 0–5 SCCM with accuracy ± (0.8% of reading +0.2% of full scale), respectively, Alicat Scientific) and mixed into a single feed stream. A downstream flow meter (0–5 SLPM with accuracy ± 0.6% of reading OR ±0.1% of full scale, whichever is greater, Alicat Scientific) is used to confirm the flow rate through each individual reactor.

Supplying a single gas stream to the system reduces the complexity of flow controllers and ensures minimal inter-reactor gas composition variability. Yet, this requires the ability to precisely divide the stream across the array of reactors. To accomplish this passively, the flow resistance (*i.e.*, pressure drop at a given flowrate, which is primarily a function of catalyst bed resistance) of each leg (analogous to parallel electrical resistors) needs to be matched. In CASHD, this was accomplished through the addition of a flow resistor upstream of each reactor with a sufficiently high resistance (much greater than the catalyst bed, around 1 atm above ambient) to minimize the flow variability attributed to the catalyst (Fig. S3). In addition, a needle valve on each leg was used to fine-tune or balance these flow resistors at the beginning of each screening experiment (less than ±2% of the nominal flow rate).

Temperature control. Eight furnaces were built to operate at independent temperature setpoints (Fig. S4). The temperature was controlled using a K-type thermocouple (DwyerOmega TJ36-CASS-116U-18-SB-SMPW-M) placed 2 mm above the top of the catalyst bed (Fig. S2). Note that this is an important distinction from traditional tube furnaces, which are typically controlled *via* thermocouples mounted outside of the reactor tube. The heater was controlled using a PID (proportional-integral-derivative) temperature controller

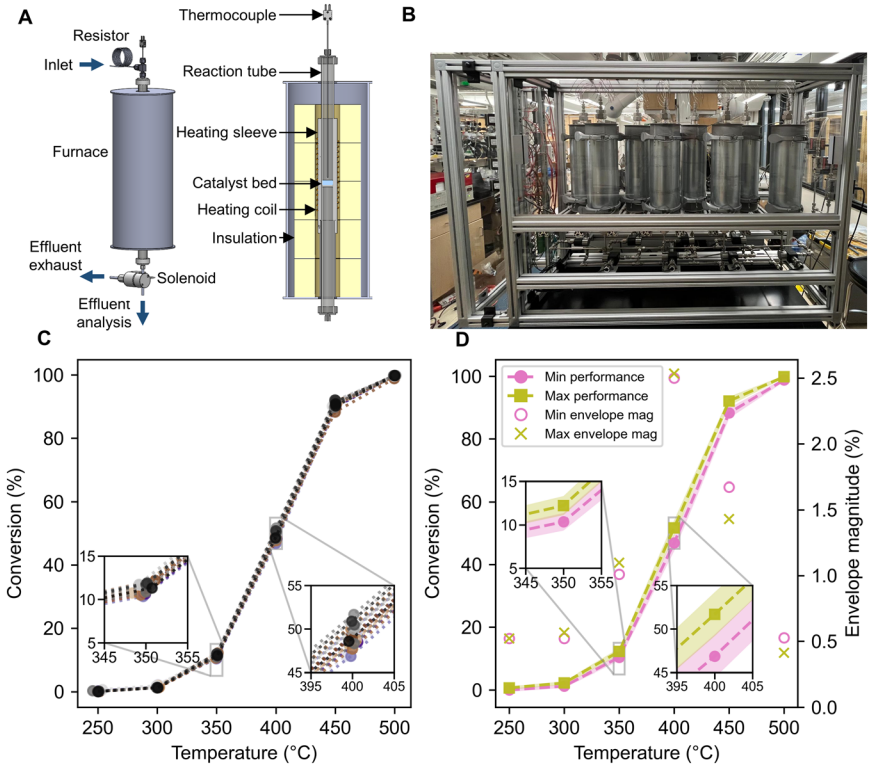

Fig. 1 Schematic, photograph, and uncertainty quantification of the catalytic array for high-throughput screening and discovery (CASHD). (A) Schematic design of one reactor. The left view is a dimetric projection with flow paths (indicated by blue arrows) and external components labeled and the right view is a cross-section with internal components labeled. (B) Fabricated device with gas flow, temperature, and valve control. A range of flow rates (0.5–1000 SCCM per reactor), methane concentrations (1 ppm–10%), and temperatures (25–600 °C) can be tested autonomously. (C) Light-off curves of the same catalyst in each reactor tested three times, where each line represents a different experiment (additional details in Fig. S7). (D) Uncertainty envelope applied to the maximum and minimum performance light-off curves from all eight reactors. The envelope magnitude for the maximum performance and minimum performance light-off curves are also plotted and designated as max envelope mag and min envelope mag in the legend, respectively. The light-off curves were measured at 1000 ppm methane in 100 SCCM dry air with 1.0 g of 2.8 MOR catalyst. Lines are to guide the eye; shading represents the uncertainty envelope.

(DwyerOmega CN-402) interfaced with a solid-state relay (McMaster-Carr 7456K21) to convert the control signal into a heating cycle and with feedback from the thermocouple to achieve a temperature setpoint in the range of 30–600 °C. The heaters were all controlled remotely using RS-485 serial communication protocol and a custom Python script (included in the SI).

Effluent valve control and analytical measurement. Effluent gases from each reactor were monitored *via* a cavity ring-down spectrometer (CRDS) by sequentially opening a single three-way solenoid valve placed downstream of each reactor while the remaining seven three-way solenoid valves were closed. When the solenoids were closed, the corresponding furnace effluent streams went to exhaust. The timing and state of the solenoids were controlled by a microcontroller (Arduino Mega) and an auxiliary crystal oscillator real-time-clock for component synchronization (Fig. S5). The effluent sent to analysis was first directed through the flow meter and then delivered to a Picarro G2201-i CRDS that measured the concentration and δ^{13}-C_{VPDB} signature of methane and carbon dioxide every 5 seconds. The analyzer was operated in CH_4 and CO_2 simultaneous high dynamic range mode. The operational range for methane and carbon dioxide were 1.8–1500 ppm and 100–4000 ppm, respectively.

Uncertainty quantification. Estimating uncertainty was crucial for evaluating the reactor itself and enabled rapid screening by reducing the need for triplicate measurements on reaction data. To quantify CASHD's variability, light-off curves of the same 2.8 wt% Cu mordenite (different samples from the same batch) were run in each of the eight reactors at three separate times, resulting in 24 total light-off curves. The variance components used for uncertainty quantification across light-off curve screening experiments were associated with the experiment number (σ_u^2), reactor number (σ_r^2), and a residual component (σ_ε^2; *e.g.*, capturing analytical error). These components encompassed the experiment-to-experiment variability, the reactor-to-reactor variability, and the remaining instrument variability, respectively. A two-way crossed random-effects ANOVA with method-of-moments was used to calculate these components.[34] A variance components model (eqn (1)) was analyzed to determine the pieces of uncertainty as well as the total uncertainty at a given conversion.

$$y_{ij} = m + r_j + u_i + \varepsilon_{ij} \quad (1)$$

where y was the conversion at some reactor (j = 1–8), experiment (i = 1–3) pair, which was modeled as the average value (m) across all observations and random effects of reactor (r), experiment (u), and residual error (ε). In this model, interaction was absorbed by the residual component because there was only one observation within a reactor and experiment pair. The variance components were determined through method of moments which equates the expected and observed mean squares (eqn (2)–(4)).

$$\sigma_\varepsilon^2 = \frac{\sum_{i=1}^{3}\sum_{j=1}^{8}\left(y_{ij} - \bar{y}_{i.} - \bar{y}_{.j} + \bar{y}_{..}\right)^2}{14} \quad (2)$$

$$\sigma_r^2 + \frac{\sigma_\varepsilon^2}{3} = \frac{\sum_{j=1}^{8}\left(\bar{y}_{.j} - \bar{y}_{..}\right)^2}{7} \quad (3)$$

$$\sigma_u^2 + \frac{\sigma_\varepsilon^2}{8} = \frac{\sum_{i=1}^{3}\left(\bar{y}_{i.} - \bar{y}_{..}\right)^2}{2} \quad (4)$$

where $\bar{y}_{i.}$ is the mean of all y_{ij} for a given i, $\bar{y}_{.j}$ is the mean of all y_{ij} for a given j, and $\bar{y}_{..}$ is the mean of all y_{ij}. These variance components were then solved for and assembled for future unknown observations (eqn (5)).

$$\sigma^2_{\text{predicted}} = \sqrt{\sigma_r^2 + \sigma_u^2 + \sigma_\varepsilon^2} \quad (5)$$

An uncertainty envelope with a 95% predicted confidence interval was determined and used in the catalyst screening experiment by multiplying the $\sigma^2_{\text{predicted}}$ by the critical value from a Student's t-distribution (eqn (6)).

$$y_{\text{predicted}} = y_{\text{new}} \pm 2.145\sigma_{\text{predicted}} \quad (6)$$

Catalyst preparation

Four zeolite frameworks were purchased in ammonium form from Zeolyst: mordenite (MOR), beta (BEA), ferrierite (FER), and ZSM-5 (MFI). Similar Si/Al ratios of 10 (MOR), 12.5 (BEA), 10 (BEA), and 11.5 (MFI) were used. Copper nitrate trihydrate (Thermo Scientific, 99%) solutions between 6–466 mM (750 mL) were made in 18 MOhm water to tune the copper loading. Zeolite powder (15.00 ± 0.01 g) was added to the copper nitrate solution and mixed for 24 h. Post-exchange preparation was conducted according to a procedure reported previously.[7] The particle sizes used in all reactions were between 106 and 500 μm. Copper loading was determined through inductively coupled plasma optical emission (ICP-OES) after complete acid digestion both of which were conducted by Galbraith Laboratories. Digestion and ICP-OES details can be found in the SI. The catalyst naming convention in subsequent sections takes the form "weight percent copper framework code" (*e.g.*, 1.9 MOR is mordenite doped to a final weight percent of 1.9% Cu). Note in ion-exchange it is inherently difficult to determine the copper loading *a priori* and thus metal loadings are close to but not exactly at nominal loading levels of 1.5, 2.5, 3.5 and 4.5 wt%.

Catalysis

Catalyst screening. 500 mg of prepared catalyst was loaded into CASHD and activated in continuously flowing (100 SCCM) dry air (Linde AI-0.0UZT) for one hour at 450 °C. Methane (Linde ME 3.7UH-T) was introduced at 1000 ppm, blank values were recorded prior to light-off curve initiation. The temperature was varied from 250 to 500 °C in steps of 25 °C. The total flow rate remained at 100 SCCM for the entire experiment. Space time through the catalyst total bed volume, calculated at the inlet conditions, ranged between 0.9 and 1.7 seconds (GHSV of 3800 and 2100, respectively). Note that since only one device (CRDS) was used to measure the methane concentration, coordination between system components and switching of reactors was necessary. Each reactor was directed to the CRDS continuously for five minutes after at least 15 minutes of equilibration at every hour-long temperature step. The first three minutes of measurement were used to flush the effluent tubes and the last two minutes of measurement were recorded, averaged, and reported on the light-off curve.

Kinetic testing. Experiments to determine the activation energy and reaction order of the catalysts were conducted at differential conditions (conversion <10%). The absence of internal and external mass transfer effects was verified through the Mears and Weisz–Prater dimensionless criteria (Tables S2 and S3). Each of the 16 catalysts (500 ± 1 mg) was loaded into CASHD and activated for one hour at 450 °C in dry air then cooled to the first temperature of kinetic testing. The total flow was kept constant at 1000 SCCM. Reaction order experiments and Arrhenius experiments were conducted in triplicate at methane concentrations between 12 and 1200 ppm and temperatures between 290 and 390 °C. Each replicate was tested in a different reactor; 30 minutes of thermal equilibration followed each temperature step and an *in situ* blank measurement was collected twice each hour. Reported uncertainty on the apparent activation energy and methane orders were derived from the standard error on the fit slope. Statistical significance between catalyst pairs was evaluated with a two-sided p-value of the Welch t-test to populate a significance matrix for catalyst comparison.

In situ optical spectroscopy

Diffuse reflectance ultraviolet-visible (DR UV-vis) spectroscopy was conducted on a custom-built *in situ* set-up. A high-temperature 6-around-1 optical fiber reflection probe (Avantes FCR-C-7UV400-2-BX-6X678-HTX; 200–800 nm) was embedded in a standalone reactor (*i.e.*, not part of CASHD) directly above the catalyst bed. A UV-vis lamp (Ocean Insight DH-2000-BAL, 210–2500 nm) was connected to one port of the probe and a spectrometer (Ocean Insight Flame-S-XR1-ES, 200–1025 nm) was connected to the other port (Fig. S6).

Spectra were collected at temperature (400 °C) after one hour in dry air at 100 SCCM to simulate the activation process. 30 spectra with integration time of 5 s and boxcar width of 5 nm were averaged to calculate the reported spectra. The reflected light intensity of barium sulfate was measured and used as a 100% reflection reference for calculating reflectance.

Results and discussion

Reactor system development and validation

The high-throughput reactor, CASHD, was designed and built with the goal of performing facile inter-reactor comparison as a means of catalyst screening (Fig. 1A and B). To demonstrate the consistency between reactors, a 2.8 MOR catalyst was tested in triplicate across all eight reactors. The 24-total corresponding light-off curves (Fig. 1C) showed a high degree of overlap, consistent with uniform and repeatable temperature and flow control across all eight reactors and across separate reaction runs. Despite a high degree of visual similarity, there was slight variation between different runs and reactors. The standard deviation of conversion increased from low temperatures up to a maximum (±1.2%) at the inflection point of the light-off curve and then decreased back towards zero, as temperature and conversion increased further. The standard deviation values of conversion were 0.1, 0.2, 1.2, 0.8 and 0.2% observed at 300, 350, 400, 450, and 500 °C, respectively. The overall low variation across the reactors and experiments demonstrates the utility of CASHD for high-throughput catalyst screening.

To quantify the interoperability and reproducibility of the reactor array, an uncertainty envelope was constructed with the components of variance (Table S4) from initial benchmarking experiments (Fig. 1C). The envelope, representing the 95% predicted confidence interval, was constructed as a function of conversion instead of temperature to retain applicability to different catalysts. The envelope's maximum uncertainty (±2.6% conversion) occurred at 49.2% conversion. At higher (90.8%) and lower (11%) conversions, the envelope decayed to ±1.6 and 1.1%, respectively. To demonstrate the utility of this technique, this envelope was applied to the lowest temperature (maximum performance) and highest temperature (minimum performance) light-off curves (Fig. 1D) generated from all eight reactors. Comparing these minima and maxima, the data exhibited overlapping uncertainty envelopes, suggesting that there is good intercomparability between individual reactors. This approach bounds the degree of confidence that can be applied to a given experiment, particularly when the operator does not wish to sacrifice throughput for experimental replicates. The uncertainty envelope was used in the subsequent screening experiments to highlight catalyst performance differences and to accelerate the materials discovery process. This uncertainty envelope is applicable to catalysts with similar performances but some caution should be taken when evaluating catalysts with notably different activation energies, as the catalyst used for the envelope's construction will implicitly influence the absolute amount of uncertainty. For qualitative screenings where the primary objective is to rank the performance of several catalysts, a light-off curve with an uncertainty envelope developed from one set of reactor intercomparisons may suffice since few parameters are being extracted from the data. However, for more mechanistic studies involving the extraction of kinetic parameters, the authors recommend replication of tests in order to measure uncertainty explicitly. Having constrained uncertainty in screening experiments, the tool was applied to evaluate catalyst performance *via* intercomparison across an experimental matrix of variable copper-loading within distinct zeolite frameworks.

Methane oxidation catalyst screening

The type of zeolite framework and copper loading were systematically varied to test CASHD's capability to generate data for catalyst inter-comparison for methane conversion. Light-off curves were developed for 16 catalyst-loading combinations consisting of the four zeolite frameworks, each at four copper loadings. Performance was evaluated *via* T_{50} (the temperature at 50% conversion), a metric widely used to describe a light-off curve's position with respect to temperature and, consequently, catalyst activity.[35,36] Across all zeolite frameworks, performance increased monotonically with copper loading (Fig. 2). The 4.3 MFI and 3.5 MFI catalysts showed the lowest T_{50} values across all catalysts (T_{50} values of 366 and 374 °C, respectively), whereas the 1.9 MFI and 2.5 MFI catalysts had notably higher T_{50} values (429 and 400 °C, respectively) that were in the range of the worst performing Cu-loadings of FER and MOR (1.8 and 2.7 FER had T_{50} values of 431 and 406 °C, respectively, and 1.9 and 2.7 MOR had T_{50} values of 413 and 407 °C, respectively). The BEA framework had the lowest activity across all catalysts regardless of copper loading (1.9, 2.5, 3.4, and 5.0 BEA had T_{50} values of 505, 471, 460, and 441 °C, respectively). MOR and FER showed intermediate but consistent behavior across the catalysts tested and T_{50} values were clustered closer to the MFI catalysts than BEA, as shown by the overlapping T_{50} values for FER, MFI, and MOR. The spread of T_{50} values between the highest and lowest copper loading for each catalyst was lower for MOR (spread of 27 °C) than for FER (46 °C), MFI (53 °C), and BEA (64 °C). Additionally, the slope of the light-off curve at T_{50} was more consistent across copper levels for MOR (0.86 to 0.89% $°C^{-1}$) and FER (0.76 to 0.85% $°C^{-1}$), whereas BEA and MFI displayed a larger increase in slope with increasing copper loading (0.58 to 0.75% $°C^{-1}$ for BEA and 0.56 to 0.92% $°C^{-1}$ for MFI). The consistency in the MOR and FER curve shape resulted in a high degree of overlap in the uncertainty envelopes. The highest loadings of FER, 3.7 FER and 4.3 FER, were functionally indistinguishable from each other. Similarly, MOR showed comparable curves at low loadings (1.9, 2.7, and 3.3 wt%), with 2.7 MOR showing envelope overlap with both 1.9 and

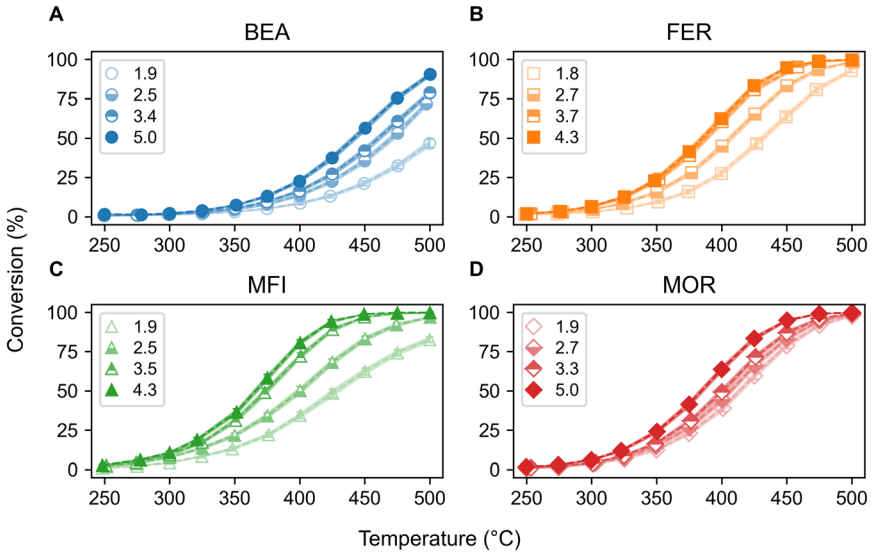

Fig. 2 Methane oxidation light-off curves for copper zeolites. Frameworks (A) BEA, (B) FER, (C) MFI, and (D) MOR were evaluated, where the numbers in the legend correspond to measured copper loading (wt%). Experiments were run at 1000 ppm methane in dry air at 100 SCCM over 500 mg of catalyst. Dotted lines are to guide the eye; shading represents the uncertainty envelope.

3.3 MOR, but observable distinction between 1.9 MOR and 3.3 MOR. CASHD and its uncertainty envelope facilitated this rapid screening which was successful at identifying 4.3 MFI as the optimal catalyst for achieving complete methane conversion at the lowest operating temperature under the conditions tested.

The importance of metal loading was observed previously, where M'Ramadj *et al.* demonstrated an increase in methane oxidation with an increase in copper loading on a ZSM-5 (*i.e.*, MFI) zeolite support.[11] This relationship supports the hypothesis that copper is the active component for catalytic methane oxidation, and the reaction is not strictly due to the zeolite framework (see Fig. S8 for no-copper control data).[7] Nevertheless, the choice of framework exhibited a clear effect on the catalyst's reactivity (Fig. 2), suggesting that the site type, site accessibility, and/or resistance to inhibition may differ across the set of catalysts tested. The changing light-off curve shape may result from internal mass transport limitations within the zeolite particles.[37] This may be particularly true at high temperatures, when reaction rates are more likely to exceed the diffusion rate (*i.e.*, differences in reactivity are a result of differential transport rates of methane through the zeolite pore structure). In this case of internal mass transport limits, the reaction's apparent activation energy can be reduced by as much as half of the reaction's true activation energy, severely reducing the reaction's measured temperature dependence.[38] Previous work demonstrated that combustion active sites, for a palladium zeolite oxidizing methane[8] and a copper zeolite oxidizing 1-octadecene,[39] were located at variable depths in the zeolite pore structure. However, copper zeolite site types and their corresponding detectable diffusional behavior due to site location have not been explicitly studied for methane total oxidation. Future work should focus on understanding these features to elucidate site-accessibility differences and guide material development.

Kinetic evaluation of catalysts using CASHD

To better understand the relative activation barriers for these catalysts, the kinetics for all 16 catalysts were probed with triplicated Arrhenius experiments (Fig. 3A). All data was extracted from differential conversion regimes (*e.g.*, less than 10% conversion), such that the local methane concentration at any point within the catalyst bed can be approximated by the inlet concentration. To highlight CASHD's capability to quantitatively determine meaningful kinetic parameters, we no longer assumed uncertainty envelope transferability to quantify performance discrepancies but rather used standard errors derived from triplicate measurements. Apparent activation energies were explicitly measured with the aforementioned Arrhenius experiments (Table 1, where constant reaction order was verified in Fig. S9). The apparent activation energy of the reaction describes the barrier of the ensemble of processes that dictate the catalyst's reactivity (*e.g.*, adsorption and reaction steps which both contribute to the measured apparent activation energy), and provides a combination of information about the site type and species adsorption.[22,40] The measured apparent activation energy decreases from BEA (105.6 ± 14.6 to 138.3 ± 13.9 kJ mol^{-1}), to MOR (90.8 ± 6.0 to 101.8 ± 6.6 kJ mol^{-1}), to FER (85.0 ± 5.2 to 89.4 ± 6.0 kJ mol^{-1}), and finally MFI (79.8 ± 10.4 to 93.2 ± 7.9 kJ mol^{-1}), consistent with the ordering of their light off curves. We illustrated the high activation energies of BEA a with a statistical significance matrix using a Welch *t*-test ($p < 0.05$, 95% confidence level), as summarized in the significance matrix in Fig. 3B (full *p*-values in Fig. S10).

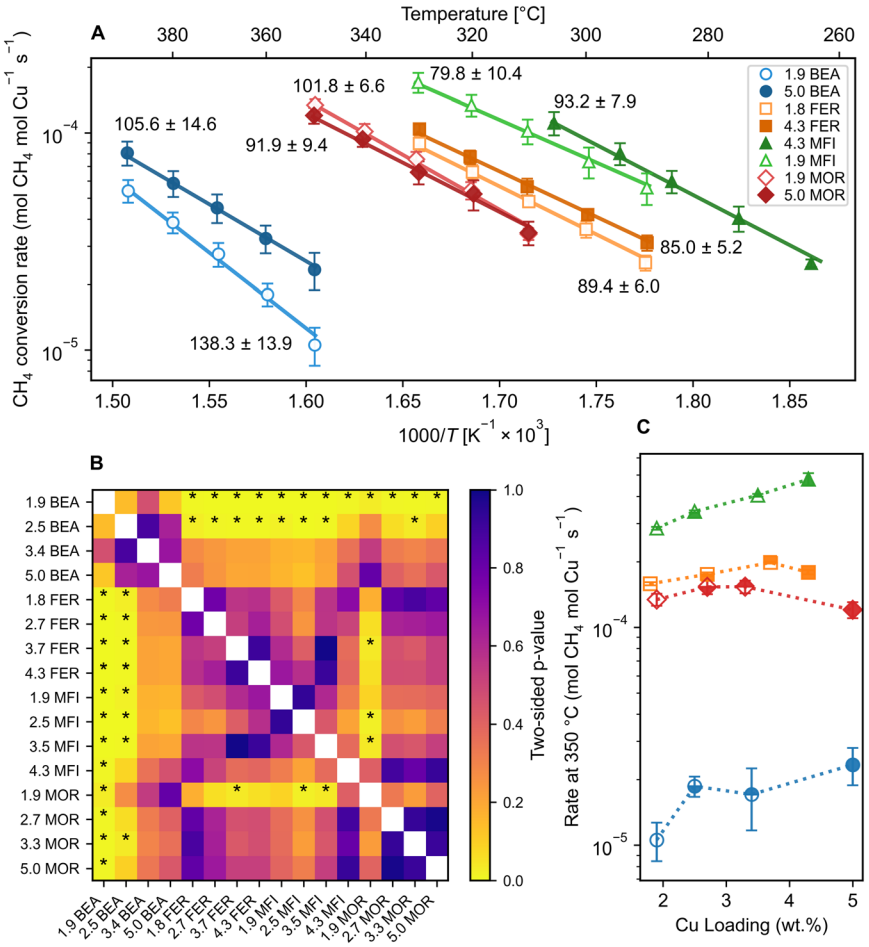

Fig. 3 Kinetic comparison of the zeolite framework type and copper loading on methane oxidation. (A) Arrhenius experiments were conducted over 500 mg of catalyst at 1000 SCCM dry air with 1200 ppm methane between 390 and 265 °C. Symbols represent the data points, lines are fit lines, and values next to fit lines are activation energies with the associated standard error in kJ mol^{-1}. Note that curves are only shown for the highest and lowest copper loadings for clarity, and the full figure is shown in the SI (Fig. S11). Order with respect to methane was verified to be consistent across the temperatures tested (Fig. S9). (B) Catalyst pairs with statistically significantly different ($p < 0.05$) activation energies evaluated by a Welch *t*-test are labeled with an asterisk, and the color in the matrix corresponds to the *p*-value magnitude. Note that the matrix shows symmetry across the diagonal but identical values are displayed to enable easier visual comparison. (C) A Madon–Boudart plot for all of the frameworks tested at their lowest metal loading (extrapolated to 350 °C by the Arrhenius equation for MFI and FER as these tests only reached max temperatures between 330 and 305 °C) showed the influence of copper loading on the reaction rate. Symbols defined in panel a apply throughout the figure and all symbols are consistent with Fig. 2.

The activation energies of the two lowest copper loading BEA catalysts, 1.9 BEA (138.3 ± 8.3 kJ mol^{-1}) and 2.5 BEA (113.8 ± 8.3 kJ mol^{-1}), were statistically different from many of the other catalysts. The activation energy of 1.9 BEA was significantly different from all MOR, FER, and MFI catalysts. Additionally, 2.5 BEA had an activation energy that was significantly different from 1.9 MFI (79.8 ± 10.4 kJ mol^{-1}), 2.5 MFI (80.8 ± 5.3 kJ mol^{-1}), 3.5 MFI (85.6 ± 2.8 kJ mol^{-1}), 3.3 MOR (90.8 ± 6.0 kJ mol^{-1}), and all FER catalysts. The only other catalyst that had a different activation energy compared with more than three catalysts was 1.9 MOR (101.8 ± 6.6 kJ mol^{-1}). This catalyst was significantly different from 1.9 BEA, the catalyst with the highest activation energy, and 3.7 FER (85.6 ± 2.4 kJ mol^{-1}), 2.5 MFI, and 3.5 MFI, three catalysts with relatively low activation energies. Importantly, within a framework type there were no significant differences in activation energy across copper loadings. This suggests that the differences in catalytic mechanism and/or active site identity between zeolites stem from differences in their crystal structure more than copper loading. While comparison of activation energies is useful for determining mechanistic insights, intercomparison of reaction rates may be more useful for practical extensions (*e.g.*, designing reactors or selecting optimal performance).

Examining the rate of reactant transformation per mole of metal as a function of metal loading (Madon–Boudart experiment)[41] has both been used to confirm the absence of intraparticle diffusion when metal dispersion remains consistent[42] and to bolster claims of site type changes in dynamic catalysts like metal-doped zeolites.[8] Comparison of the copper-normalized reaction rates revealed more than an order of magnitude performance increase (*i.e.*, 18 to 27 times

Table 1 Channel system, chemical composition, water absorption capacity, specific surface area, and performance metrics of the zeolites catalysts used in this study

Material	IZA code	Channel System[a]	Si/Al[b]	SA[b] ($m^2\ g^{-1}$)	Water ads.[c] ($g\ g_{zeolite}^{-1}$)	Wt% Cu	T_{50} (°C)	E_a[d] (kJ mol^{-1})	Order[d]
Beta	BEA	12-ring	12.5	680	0.213	1.9	505	138 ± 14	0.75 ± 0.03
						2.5	471	114 ± 8	0.77 ± 0.04
						3.4	460	118 ± 24	0.75 ± 0.04
						5.0	441	106 ± 15	0.76 ± 0.04
Mordenite	MOR	12- and 8-ring	10	500	0.150	1.9	413	102 ± 7	0.78 ± 0.02
						2.7	407	92 ± 8	0.76 ± 0.02
						3.3	401	91 ± 6	0.72 ± 0.02
						5.0	384	92 ± 9	0.70 ± 0.03
Ferrierite	FER	10- and 8-ring	10	400	0.090	1.8	431	89 ± 6	0.80 ± 0.02
						2.7	406	88 ± 2	0.75 ± 0.00
						3.7	388	86 ± 2	0.70 ± 0.01
						4.3	385	85 ± 5	0.70 ± 0.02
ZSM-5	MFI	10-ring	11.5	425	0.068	1.9	428	80 ± 10	0.88 ± 0.02
						2.5	400	81 ± 5	0.78 ± 0.02
						3.5	374	86 ± 3	0.75 ± 0.01
						4.3	366	93 ± 8	0.71 ± 0.04

[a] Channel system referenced from Database of Zeolite Structures. [b] Referenced from Zeolyst International product specifications. [c] Aggregated from Tatlier *et al.*[48] [d] Uncertainty from standard error of the fit slope.

larger rates at comparable copper loadings) spanning BEA to MFI. Interestingly, MFI was the only framework that showed a monotonic increase in the copper-normalized reaction rate. MOR, FER, and BEA all showed variable but relatively consistent copper-normalized reaction rates. This indicates that the dominant site type may have remained consistent for MOR, FER, and BEA, whereas for MFI a shifting site distribution may be responsible for the larger effect of copper loading on catalyst reactivity. In the context of other work, nonlinear site distributions as a function of metal loading have been reported for copper-exchanged zeolites.[43] It is also worth noting that intraparticle diffusion limitations in these experiments was unlikely because the measured activation energies did not show a meaningful decrease (limit of $E_a/2$) with metal loading.

Previous literature on methane total oxidation catalysts has shown similar activation energies to those reported here. Dry and wet methane oxidation over palladium catalysts has been reported to have apparent activation energies from 66 to 87 kJ mol^{-1} and from 125 to 179 kJ mol^{-1}, respectively.[8,44–46] Reports of activation energies for copper catalysts are limited, but copper-exchanged zeolites for PMO have been shown to have relatively low measured activation energies between 33 and 66 kJ mol^{-1}, dependent on the dominant site type.[22,47] In this work, BEA exhibited generally higher activation energies, followed by MOR, then FER, then MFI. This ordering corresponds to the relative water adsorption capacities of the frameworks (0.213, 0.150, 0.090, and 0.060 $g_{water}\ g_{zeolite}^{-1}$).[48] This may suggest that water generated from the oxidation process played a disproportionate role in BEA catalytic activity. Such an effect would be pronounced when the reaction is run at dry conditions (*i.e.*, no water vapor is added to the influent stream), as in these experiments. Other intercomparable properties of the zeolite frameworks, such as channel system, silicon-to-aluminum ratio, and the surface area, do not have any noticeable differences that correspond to the relative ordering of framework performance (Table 1) that can be quantitatively evaluated. BEA is a 12-ring assembly, MOR contains 12- and 8-ring, FER contains 10- and 8-ring, and MFI contains a 10-ring structure. The Si/Al ratios in this study were purposefully close (12.5, 10, 10, 11.5 for BEA, MOR, FER, and MFI, respectively), and the relative surface area ordering did not follow the same rank ordering as activation barrier observations (680, 500, 400, and 425 $m^2\ g^{-1}$, respectively). Interestingly, despite the wide range of performances across the frameworks and copper loadings tested, the reported reaction order (Table 1) with respect to methane stays relatively consistent (*i.e.*, a range of 0.71 ± 0.04 to 0.88 ± 0.04), which suggests that the methane adsorption on the active site could have followed similar behavior across the distinct catalysts if the reaction mechanism was dependent on fractional site coverage (*i.e.*, Langmuir–Hinshelwood or Eley–Rideal). A Langmuir–Hinshelwood mechanism is potentially more plausible due to the previously reported zeroth order dependence on oxygen partial pressure[8,49] in dilute methane oxidation and the fractional methane order reported here. This may indicate that oxygen (high site coverage) and methane (intermediate site coverage) adsorption are both important and thus the reaction proceeds through a Langmuir–Hinshelwood mechanism.

The general effect of metal loading on reaction rate for combustion catalysts has been documented previously. The optimum loading (*i.e.*, the loading resulting in the maximum per-gram-of-catalyst reaction rate) and what inhibits further return on reactivity as loading is increased can vary widely depending on the metal and support structure used.[8,50] Losch *et al.* found that increasing the palladium loading past 0.5 wt% constricted zeolite pores in ultra-stable Y (USY), BEA,

and MFI.[50] Cui *et al.* found the effect of increasing the palladium loading in SSZ-13 from 0.2 to 2 wt% resulted in a more than three orders of magnitude rate increase,[8] but diminishing returns when the loading was increased to 2 wt%, potentially due to a reduction in copper dispersion. There was then a steady increase in the per-gram-of-catalyst reaction rate up to the maximum tested 5 wt%.[8] In this study, copper loading had a more modest effect across a broad range of metal loading (1.9–5.0%), while framework type resulted in an order of magnitude rate increase (Fig. 3C). It is worth noting that at 350 °C MFI had both the highest reported rate per mole of copper across all copper loadings and a positive slope on the Madon–Boudart plot. This indicates a higher per-gram-of-catalyst rate could be achieved at higher copper loadings.

In situ characterization of catalysts

Catalyst characterization *via* DR UV-vis spectroscopy. *In situ* spectroscopic techniques have been widely used in catalysis to non-invasively measure materials during reaction conditions.[14,18,22,51] DR UV-vis is particularly useful for probing transition metal catalysts, as it is robust and provides rapid assessment relative to other spectroscopic techniques such as, X-ray diffraction (XRD) and X-ray absorption spectroscopy (XAS).[52] A ninth reactor tube was constructed to enable DR UV vis, spectra (Fig. 4) were measured for each catalyst after activation in dry air. In future work we envision integrating DR UV-vis across all eight reactors in CASHD. Across all catalysts tested, increasing copper loading generally led to higher attenuation across all wavenumbers (12 500–45 000 cm^{-1}). Additionally, broad bands at 42 000 and 13 000 cm^{-1} were seen across all catalysts, corresponding to the ligand–metal charge transfer and d-d regions, as have been observed for other ion-exchanged copper zeolite catalysts.[15,18,22,23,51,53] However, these same studies consistently report a 22 000 to 26 000 cm^{-1} band, often attributed to the copper mono-(μ)-oxo dimer, that was absent from the reported spectra in this study. Several hypotheses may explain the absence of this band: residual water may have hydrolyzed dimers upon dimer formation,[54,55] dimers may not have formed at all due to a lack of the hypothesized precursor Cu^{+},[56] domination of the spectra by isolated monomers (Z_2Cu),[51] or obfuscation by the broad background attenuation of nanoclusters or nanoparticles.[15]

Enhanced curvature in the reflection spectra was seen near 27 000 cm^{-1} as copper loading increased for BEA, but assignment of this feature was difficult due to a dearth of UV-vis data on copper-exchanged BEA. MFI showed the most noticeable change in attenuation when increasing copper loading. The curvature changed the most between 2.5 and 3.5 and occurred primarily at wavenumbers between 10 000 and 30 000 cm^{-1}. This broad attenuation in the intermediate wavenumber region has been attributed to nanoparticle formation.[15,57] The lack of evidence of Cu dimers *via* DR UV-vis, combined with the reaction kinetics, indicates that Cu dimers might not be necessary at these conditions (unlike PMO where they have been confirmed to

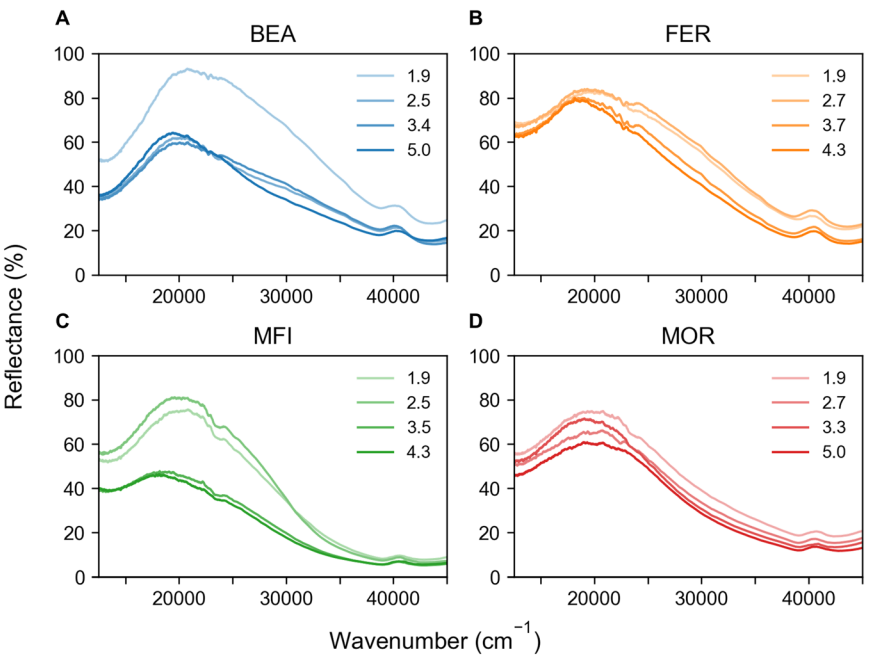

Fig. 4 Diffuse reflectance spectra of UV-vis light for various copper-doped zeolites. Spectra were collected *in situ* after a one hour activation at 400 °C in continuously flowing dry air without methane. All 16 catalysts were measured and are grouped by zeolite framework (A) BEA, (B) FER, (C) MFI, and (D) MOR, where the numbers in the legend correspond to measured copper loading (wt%). The diffuse reflectance probe was embedded in the reactor directly above the catalyst. Light attenuation at various wavenumbers as a function of copper loading is shown in the SI (Fig. S12).

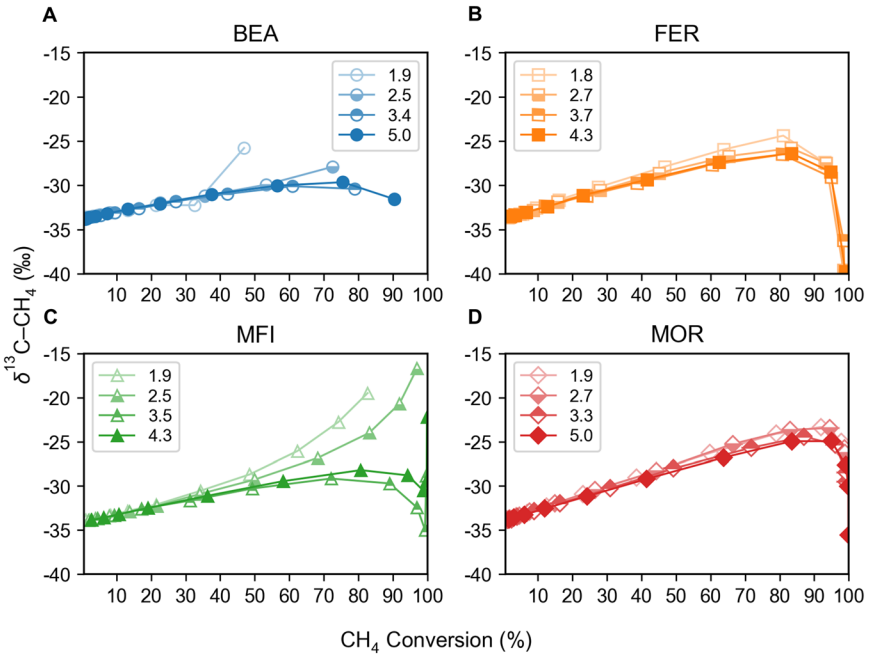

Fig. 5 Isotopic fraction of ^{13}C and ^{12}C in the residual methane due to the catalytic oxidation over various copper-doped zeolites. Frameworks (A) BEA, (B) FER, (C) MFI, and (D) MOR were evaluated, where the numbers in the legend correspond to measured copper loading (wt%). Data were collected during light-off curve experiments at 1000 ppm methane in dry air, and the conversion scale corresponds to progressively increasing reaction temperatures. Methane starting composition of −34‰ was measured at 0% conversion.

be necessary).[17,21–24] However, Cu dimers activity for methane oxidation should not be completely disregarded as there still may be a path to lower temperature complete oxidation activity that leverages these sites. Future studies could explore this systematically *via* variable preparation techniques favoring formation of the distinct active site morphologies and rapid screening on CASHD.

Effluent gas characterization *via* isotopic abundance. Many heterogeneous catalysis reactor systems characterize the effluent gas composition *via* gas chromatography, which relies on injection of discrete packets of gas onto a separatory column which then feeds into a detector. In this high-throughput system, the use of a Picarro CRDS tool allowed for continuous characterization of both gas concentration as well as the isotopic abundance (^{13}C-to-^{12}C ratio). The isotopic abundance of the residual methane reflected differences across catalyst types, even though the influent methane was derived from the same source throughout (Fig. 5). This indicates that isotopic fractionation occurred differentially as a function of catalyst type, allowing for further investigation into active site types or physical transport through the frameworks. Measurement of isotopic abundance of ^{13}C is one of the unique capabilities of CASHD when integrated with a Picarro G2201-i. By convention, isotopic ratios are reported using $\delta^{13}C$ notation, which normalizes small differences in the ^{13}C to ^{12}C ratio of a sample to that of a reference material (eqn (7)), where the scale is defined by the reference material Vienna Pee Dee Belemnite (VPDB) with a ^{13}C:^{12}C of 0.011113.

$$\delta^{13}C_{sample}(‰) = \left(\frac{(^{13}C/^{12}C)_{sample} - (^{13}C/^{12}C)_{VPDB}}{(^{13}C/^{12}C)_{VPDB}}\right) \times 1000 \quad (7)$$

Fractionation of a reactant from its starting isotopic composition can result from a variety of phenomenon, such as kinetic isotope enhancement (KIE), equilibrium isotope enhancement (EIE), and diffusional enhancement. KIE and diffusional enhancement usually result in the preferential reaction of the light isotope due to differences in either transition state energies or diffusion between the heavy and light isotopes. EIE often results in the preferential reaction of the heavy isotope if the surface adsorption phenomena resulted in a more strongly bound ^{13}C.[58]

Measurement of the isotopic composition of the residual methane showed an increasing residual methane $\delta^{13}C$ with increasing conversion (Fig. 5) up to 60% conversion for all catalysts. The increase in $\delta^{13}C$ (*i.e.*, enrichment) in the remaining unreacted methane, meant more of the $^{12}CH_4$ was oxidized than $^{13}CH_4$. Across all copper loadings, FER and MOR showed very similar $\delta^{13}C$ profiles over concentration. The average maximum $\delta^{13}C$ for FER and MOR was −26 and −24 ‰, respectively. The more prominent difference for FER and MOR was that the average maximum $\delta^{13}C$ value was observed at different total conversions; 92% and 82% conversion for MOR and FER, respectively. The apparent sharp depletion at high conversion rates for MOR and FER may be a consequence of the near total conversion, translating to very low methane levels that approach the

limits of Picarro CRDS sensitivity (limit of detection of $^{12}CH_4$ is 1.8 ppm); if BEA and MFI where tested to these extreme conversions, the isotopic abundance as a function of total conversion would likely show the same behavior. BEA and MFI, the least and most reactive catalysts, exhibited different isotopic fractionation trends as compared to MOR and FER. BEA had a more gradual increasing $\delta^{13}C$ trend as conversion increased across copper loading, with 3.4 and 5.0 wt% reaching a maximum $\delta^{13}C$ of −30‰. The low copper loadings of BEA at 500 °C (the highest measured conversion) began to deviate from the trajectory of the higher loadings with 1.9 BEA reaching −26‰ and 2.5 BEA reaching −28‰. The most striking differences were observed for MFI, which displayed similar $\delta^{13}C$ trends across copper loadings up to 35% conversion. At higher methane conversions, 1.9 MFI and 2.5 MFI inflected upwards, reaching a maximum value of −19‰ and −17‰, respectively, suggesting that a unique mode of fractionation dominated the isotopic abundance measurements of these two catalysts.

The upward inflection in both BEA and MFI could result from the onset of diffusion limitations. However, due to the multiple drivers of fractionation, further characterization would be required to build evidence in support of a particular dominant mechanism. To date, no other methane oxidation studies used natural abundance of ^{13}C to assess diffusional or kinetic enhancement (one study used a ^{13}C tracer in PMO to confirm catalytic turnover on the copper active sites).[59] Isotope tracer studies obfuscate any fractionation effects due to the overwhelming presence of a single isotope. Here, the highly variable fractionation across copper loading in the MFI isotopic abundance plots could plausibly result from a diffusional effect. This is partially supported by the screening experiment (Fig. 2C), which may have shown a diffusional effect difference at high conversions between the low (1.9 and 2.5 wt%) and high (3.5 and 4.3 wt%) loading MFI and the DR UV-vis experiment, which showed segregation of behavior between 2.5 and 3.5 MFI, potentially due to nanocluster or particle formation. Hypothesized nanoparticles could be investigated by trying to increase or decrease their formation during preparation and direct investigation of particle presence (*e.g.* with X-ray absorption spectroscopy (XAS) and transmission electron microscopy (TEM)). This, coupled with detailed batch and flow studies of the isotopic phenomenon as a function of catalyst type and proposed active sites in isolation, could be used to better constrain the underlying chemical physics driving complete methane oxidation in metal-doped zeolite catalysts.

Catalysis for greenhouse gas removal presents a unique and impactful test case for materials discovery and optimization. For dilute catalytic methane oxidation, even a marginal improvement in catalytic activity can translate to an improved net climate impact *via* a reduction in the reaction temperature.[4] Relative to other frameworks, BEA catalysts showed lower catalytic performances (*i.e.*, high T_{50} values, low reaction rates, and high activation energies) across all copper loadings, potentially due to its relatively high hygroscopicity (*i.e.*, active site blockage by water molecules or surface hydroxyls). MFI, the framework with the highest measured catalytic activity, showed potential site type changes and high-conversion diffusional limitations with increasing copper loading, highlighted primarily by the light-off curves shapes, Madon–Boudart plot, DR UV-vis spectra, and isotopic fractionation. MOR and FER appear to have consistent populations of active site type across all copper loadings, as evidenced by the uniform shape of their light-off curves, consistent activation energy across loadings, constant Cu-normalized reactivity, similar DR UV-vis spectra and uniform isotopic fractionation behavior. While this work was focused on the design and validation of CASHD, future high-throughput assessments can prioritize catalysts of interest for the development of detailed mechanistic understanding using lower throughput advanced microscopy (TEM) and spectroscopy (XRD, XAS, EPR, and NMR).

Conclusions

Overall, CASHD demonstrated its utility by screening a suite of zeolite catalysts for methane oxidation and evaluating their kinetics. Improvements to the reactor design, like increasing the number of gases that can be delivered to the reactor could allow for more mechanistic order or other reaction studies. Additionally, adding a saturator for water vapor control and measurement of residual water content in the effluent could help probe the role of water and bolster the real-world applicability of the catalyst screening and characterization. Ultimately, automatization of the catalyst dispensing and reaction tube loading would further enhance throughput and enable an additional degree of closed loop experimentation. As materials discovery and catalysis are accelerated with recent advances in machine learning and generative design, the actual physical testing of materials remains a rate-limiting step. Development of CASHD and high-throughput reactors like it helps eliminate this bottleneck, ultimately enabling the rapid discovery of critically needed catalysts or testing of a variety of structures posed by artificial intelligence-informed materials discovery.

Author contributions

EEM: experimental design and execution, investigation, data curation, and writing. WJS: design and review. KSW and AJH: discussion and review. DLP: experimental design, support, supervision and review.

Conflicts of interest

There are no conflicts to declare related to this work. DLP and AJH are co-founders of Moxair. WJS is founder of Resolute Methane.

Data availability

The data that support the findings of this study are available within the article and the supplementary information (SI).

Supplementary information: web of science "high-throughput" search comparison; furnace assembly diagram; schematic of flow control in CASHD; reaction temperature control scheme; demonstration of component synchronization; acid digestion and ICP-OES protocol; criterion for internal and external mass transfer; schematic of *in situ* DR UV-vis set-up; variance components of CASHD from benchmarking experiment; benchmarking experiment for CASHD uncertainty envelope; methane reaction orders of tested catalysts across temperature; activation energy statistical significance matrix with *p*-values; Arrhenius plots of tested catalysts; DR UV-vis light attenuation of tested catalysts at various wavenumber; temperature control program. See DOI: https://doi.org/10.1039/d6cy00033a.

Acknowledgements

This work was supported by the Department of Energy (ARPA-E #2504-1517) and the Gerstner Philanthropies. EEM was supported by the National Science Foundation Graduate Research Fellowship Program (DGE-2141064).

References

1 R. B. Jackson, E. I. Solomon, J. G. Canadell, M. Cargnello and C. B. Field, Methane Removal and Atmospheric Restoration, *Nat. Sustain.*, 2019, **2**(6), 436–438, DOI: 10.1038/s41893-019-0299-x.

2 D. P. van Vuuren, E. Stehfest, D. E. H. J. Gernaat, M. van den Berg, D. L. Bijl, H. S. de Boer, V. Daioglou, J. C. Doelman, O. Y. Edelenbosch, M. Harmsen, A. F. Hof and M. A. E. van Sluisveld, Alternative Pathways to the 1.5 °C Target Reduce the Need for Negative Emission Technologies, *Nat. Clim. Change*, 2018, **8**(5), 391–397, DOI: 10.1038/s41558-018-0119-8.

3 I. B. Ocko, T. Sun, D. Shindell, M. Oppenheimer, A. N. Hristov, S. W. Pacala, D. L. Mauzerall, Y. Xu and S. P. Hamburg, Acting Rapidly to Deploy Readily Available Methane Mitigation Measures by Sector Can Immediately Slow Global Warming, *Environ. Res. Lett.*, 2021, **16**(5), 054042, DOI: 10.1088/1748-9326/abf9c8.

4 S. Abernethy, M. I. Kessler and R. B. Jackson, Assessing the Potential Benefits of Methane Oxidation Technologies Using a Concentration-Based Framework, *Environ. Res. Lett.*, 2023, **18**(9), 094064, DOI: 10.1088/1748-9326/acf603.

5 J. Oh, A. Boucly, J. A. Bokhoven, L. Artiglia and M. Cargnello, Palladium Catalysts for Methane Oxidation: Old Materials, New Challenges, *Acc. Chem. Res.*, 2023, **57**(1), 23–36, DOI: 10.1021/acs.accounts.3c00454.

6 A. C. Parker, W. J. Sawyer, K. A. Riedinger, N. A. Bugher, A. J. Hart and D. L. Plata, Dairy Barn Methane Levels and Feasibility of Thermal Catalytic Oxidation for Net Climate Benefit, *Environ. Sci. Technol.*, 2025, **59**(49), 26428–26439, DOI: 10.1021/acs.est.5c06595.

7 R. J. Brenneis, E. P. Johnson, W. Shi and D. L. Plata, Atmospheric- and Low-Level Methane Abatement via an Earth-Abundant Catalyst, *ACS Environ. Au*, 2022, **2**(3), 223–231, DOI: 10.1021/acsenvironau.1c00034.

8 Y. Cui, J. Zhu Chen, B. Peng, L. Kovarik, A. Devaraj, Z. Li, T. Ma, Y. Wang, J. Szanyi, J. T. Miller, Y. Wang and F. Gao, Onset of High Methane Combustion Rates over Supported Palladium Catalysts: From Isolated Pd Cations to PdO Nanoparticles, *JACS Au*, 2021, **1**(4), 396–408, DOI: 10.1021/jacsau.0c00109.

9 Y. H. Ahmad, A. T. Mohamed, K. A. Mahmoud, A. S. Aljaber and S. Y. Al-Qaradawi, Natural Clay-Supported Palladium Catalysts for Methane Oxidation Reaction: Effect of Alloying, *RSC Adv.*, 2019, **9**(56), 32928–32935, DOI: 10.1039/c9ra06804j.

10 A. W. Petrov, D. Ferri, F. Krumeich, M. Nachtegaal, J. A. van Bokhoven and O. Kröcher, Stable Complete Methane Oxidation over Palladium Based Zeolite Catalysts, *Nat. Commun.*, 2018, **9**(1), 2545, DOI: 10.1038/s41467-018-04748-x.

11 O. M'Ramadj, B. Zhang, D. Li, X. Wang and G. Lu, Catalytic Combustion of Methane over High Copper-Loading ZSM-5 Catalysts, *J. Nat. Gas Chem.*, 2007, **16**(3), 258–265, DOI: 10.1016/S1003-9953(07)60057-7.

12 V. L. Sushkevich, D. Palagin, M. Ranocchiari and J. A. van Bokhoven, Selective Anaerobic Oxidation of Methane Enables Direct Synthesis of Methanol, *Science*, 2017, **356**(6337), 523–527, DOI: 10.1126/science.aam9035.

13 C. Paolucci, I. Khurana, A. A. Parekh, S. Li, A. J. Shih, H. Li, J. R. Di Iorio, J. D. Albarracin-Caballero, A. Yezerets, J. T. Miller, W. N. Delgass, F. H. Ribeiro, W. F. Schneider and R. Gounder, Dynamic Multinuclear Sites Formed by Mobilized Copper Ions in NOx Selective Catalytic Reduction, *Science*, 2017, **357**(6354), 898–903, DOI: 10.1126/science.aan5630.

14 A. J. Heyer, J. Ma, D. Plessers, A. Braun, M. L. Bols, H. M. Rhoda, R. A. Schoonheydt, B. F. Sels and E. I. Solomon, Spectroscopic Investigation of the Role of Water in Copper Zeolite Methane Oxidation, *J. Am. Chem. Soc.*, 2024, **146**(31), 21208–21213, DOI: 10.1021/jacs.4c06010.

15 K. T. Dinh, M. M. Sullivan, K. Narsimhan, P. Serna, R. J. Meyer, M. Dincă and Y. Román-Leshkov, Continuous Partial Oxidation of Methane to Methanol Catalyzed by Diffusion-Paired Copper Dimers in Copper-Exchanged Zeolites, *J. Am. Chem. Soc.*, 2019, **141**(29), 11641–11650, DOI: 10.1021/jacs.9b04906.

16 E. M. C. Alayon, M. Nachtegaal, A. Bodi, M. Ranocchiari and J. A. Bokhoven, Bis(μ-Oxo) versus Mono(μ-Oxo)Dicopper Cores in a Zeolite for Converting Methane to Methanol: An in Situ XAS and DFT Investigation, *Phys. Chem. Chem. Phys.*, 2015, **17**(12), 7681–7693, DOI: 10.1039/C4CP03226H.

17 E. Borfecchia, D. K. Pappas, M. Dyballa, K. A. Lomachenko, C. Negri, M. Signorile and G. Berlier, Evolution of Active Sites during Selective Oxidation of Methane to Methanol over Cu-CHA and Cu-MOR Zeolites as Monitored by Operando XAS, *Catal. Today*, 2019, **333**, 17–27, DOI: 10.1016/j.cattod.2018.07.028.

18 A. Brenig, J. W. A. Fischer, D. Klose, G. Jeschke, J. A. van Bokhoven and V. L. Sushkevich, Tracking Active Site Formation during Oxidative Activation of Copper-Exchanged Zeolites for Methane-to-Methanol Conversion, *Adv. Sci.*, 2025, **12**(13), 2413870, DOI: 10.1002/advs.202413870.

19 K. T. Dinh, M. M. Sullivan, P. Serna, R. J. Meyer, M. Dincă and Y. Román-Leshkov, Viewpoint on the Partial Oxidation of Methane to Methanol Using Cu- and Fe-Exchanged Zeolites, *ACS Catal.*, 2018, **8**(9), 8306–8313, DOI: 10.1021/acscatal.8b01180.

20 D. K. Pappas, A. Martini, M. Dyballa, K. Kvande, S. Teketel, K. A. Lomachenko, R. Baran, P. Glatzel, B. Arstad, G. Berlier, C. Lamberti, S. Bordiga, U. Olsbye, S. Svelle, P. Beato and E. Borfecchia, The Nuclearity of the Active Site for Methane to Methanol Conversion in Cu-Mordenite: A Quantitative Assessment, *J. Am. Chem. Soc.*, 2018, **140**(45), 15270–15278, DOI: 10.1021/jacs.8b08071.

21 M. A. Newton, A. J. Knorpp, V. L. Sushkevich, D. Palagin and J. A. Van Bokhoven, Active Sites and Mechanisms in the Direct Conversion of Methane to Methanol Using Cu in Zeolitic Hosts: A Critical Examination, *Chem. Soc. Rev.*, 2020, **49**(5), 1449–1486, DOI: 10.1039/C7CS00709D.

22 V. L. Sushkevich, M. Artsiusheuski, D. Klose, G. Jeschke and J. A. van Bokhoven, Identification of Kinetic and Spectroscopic Signatures of Copper Sites for Direct Oxidation of Methane to Methanol, *Angew. Chem., Int. Ed.*, 2021, **60**(29), 15944–15953, DOI: 10.1002/anie.202101628.

23 M. H. Groothaert, P. J. Smeets, B. F. Sels, P. A. Jacobs and R. A. Schoonheydt, Selective Oxidation of Methane by the Bis(μ-Oxo)Dicopper Core Stabilized on ZSM-5 and Mordenite Zeolites, *J. Am. Chem. Soc.*, 2005, **127**(5), 1394–1395, DOI: 10.1021/ja047158u.

24 J. S. Woertink, P. J. Smeets, M. H. Groothaert, M. A. Vance, B. F. Sels, R. A. Schoonheydt and E. I. Solomon, A [Cu2O]2+ Core in Cu-ZSM-5, the Active Site in the Oxidation of Methane to Methanol, *Proc. Natl. Acad. Sci. U. S. A.*, 2009, **106**(45), 18908–18913, DOI: 10.1073/pnas.0910461106.

25 J. C. Dellamorte, R. Vijay, C. M. Snively, M. A. Barteau and J. Lauterbach, High-Throughput Reactor System with Individual Temperature Control for the Investigation of Monolith Catalysts, *Rev. Sci. Instrum.*, 2007, **78**(7), 072211, DOI: 10.1063/1.2755781.

26 T. N. Nguyen, T. T. P. Nhat, K. Takimoto, A. Thakur, S. Nishimura, J. Ohyama, I. Miyazato, L. Takahashi, J. Fujima, K. Takahashi and T. Taniike, High-Throughput Experimentation and Catalyst Informatics for Oxidative Coupling of Methane, *ACS Catal.*, 2020, **10**(2), 921–932, DOI: 10.1021/acscatal.9b04293.

27 A. J. Sumner and D. L. Plata, Exploring the Hydraulic Fracturing Parameter Space: A Novel High-Pressure, High-Throughput Reactor System for Investigating Subsurface Chemical Transformations, *Environ. Sci.: Processes Impacts*, 2018, **20**(2), 318–331, DOI: 10.1039/c7em00470b.

28 P. Hazemann, D. Decottignies, S. Maury, S. Humbert, A. Berliet, C. Daniel and Y. Schuurman, Kinetic Data Acquisition in High-Throughput Fischer–Tropsch Experimentation, *Catal. Sci. Technol.*, 2020, **10**(21), 7331–7343, DOI: 10.1039/D0CY00918K.

29 T. Delrieux, S. Sharma, F. Maurer, P. Dolcet, M. Lausch, A. Zimina, C. Cárdenas, P. Lott, M. Casapu, T. Lennon Sheppard and J.-D. A. Grunwaldt, Laboratory Scale Fast Feedback Characterization Loop for Optimizing Coated Catalysts for Emission Control, *React. Chem. Eng.*, 2024, **9**(11), 2868–2881, DOI: 10.1039/D4RE00168K.

30 L. R. Smith, E. C. Kohlrausch, K. J. Aggett, Y. Chen, I. E. Gow, A. Weilhard, L. T. Norman, W. Theis, D. J. Morgan, L. Bailey, A. N. Khlobystov, J. Alves Fernandes and G. J. Hutchings, Direct Formation of the Atomic Pd-ZnO Interface by Magnetron Sputtering Primed for Methanol Production from CO2, *ACS Catal.*, 2025, **15**(17), 15502–15508, DOI: 10.1021/acscatal.5c04822.

31 J. H. Carter, T. Ye, D. G. Hewes, A. Almoteiry, K. J. Aggett, B. D. Vandegehuchte, C. J. Kiely, S. H. Taylor and G. J. Hutchings, Origin of Carbon Monoxide Formation in the Oxidative Dehydrogenation of Propane Using Carbon Dioxide, *ACS Catal.*, 2024, **14**(15), 11881–11892, DOI: 10.1021/acscatal.4c02628.

32 P. Nikolaev, D. Hooper, F. Webber, R. Rao, K. Decker, M. Krein, J. Poleski, R. Barto and B. Maruyama, Autonomy in Materials Research: A Case Study in Carbon Nanotube Growth, *npj Comput. Mater.*, 2016, **2**(1), 16031, DOI: 10.1038/npjcompumats.2016.31.

33 D. P. Tabor, L. M. Roch, S. K. Saikin, C. Kreisbeck, D. Sheberla, J. H. Montoya, S. Dwaraknath, M. Aykol, C. Ortiz, H. Tribukait, C. Amador-Bedolla, C. J. Brabec, B. Maruyama, K. A. Persson and A. Aspuru-Guzik, Accelerating the Discovery of Materials for Clean Energy in the Era of Smart Automation, *Nat. Rev. Mater.*, 2018, **3**(5), 5–20, DOI: 10.1038/s41578-018-0005-z.

34 3.2.3.2. Two-Way Crossed ANOVA, https://www.itl.nist.gov/div898/handbook/ppc/section2/ppc232.htm (accessed 2025-10-27).

35 P. Losch, W. Huang, O. Vozniuk, E. D. Goodman, W. Schmidt and M. Cargnello, Modular Pd/Zeolite Composites Demonstrating the Key Role of Support Hydrophobic/Hydrophilic Character in Methane Catalytic Combustion, *ACS Catal.*, 2019, **9**(6), 4742–4753, DOI: 10.1021/acscatal.9b00596.

36 X. Wang, X. Xu, W. Xiong, D. Ye and P. Chen, Hydrophobic modification of small pore Pd-SSZ-13 zeolites for catalytic methane combustion, *Top. Catal.*, 2024, DOI: 10.1007/s11244-024-01923-x.

37 T. Delrieux, S. Sharma, F. Maurer, P. Dolcet, M. Lausch, A. Zimina, C. Cárdenas, P. Lott, M. Casapu, T. Lennon Sheppard and J.-D. A. Grunwaldt, Laboratory Scale Fast Feedback Characterization Loop for Optimizing Coated Catalysts for Emission Control, *React. Chem. Eng.*, 2024, **9**(11), 2868–2881, DOI: 10.1039/D4RE00168K.

38 H. Scott Fogler, *Elements of Chemical Reaction Engineering*, 5th edn, 2016.

39 C. J. Wrasman, Q. Wu, A. T. To, A. J. Hill, F. G. Baddour, S. E. Habas and D. A. Ruddy, The Role of Cu Species in the

Regeneration of a Coked Cu/BEA Zeolite Catalyst, *J. Catal.*, 2024, **437**, 115639, DOI: 10.1016/j.jcat.2024.115639.

40 K. S. Westendorff, M. J. Hülsey, T. S. Wesley, Y. Román-Leshkov and Y. Surendranath, Electrically Driven Proton Transfer Promotes Brønsted Acid Catalysis by Orders of Magnitude, *Science*, 2024, **383**(6684), 757–763, DOI: 10.1126/science.adk4902.

41 R. J. Madon and M. Boudart, Experimental Criterion for the Absence of Artifacts in the Measurement of Rates of Heterogeneous Catalytic Reactions, *Ind. Eng. Chem. Fundam.*, 1982, **21**(4), 438–447, DOI: 10.1021/i100008a022.

42 J. J. Pacheco, J. A. Labinger, A. L. Sessions and M. E. Davis, Route to Renewable PET: Reaction Pathways and Energetics of Diels–Alder and Dehydrative Aromatization Reactions Between Ethylene and Biomass-Derived Furans Catalyzed by Lewis Acid Molecular Sieves, *ACS Catal.*, 2015, **5**(10), 5904–5913, DOI: 10.1021/acscatal.5b01309.

43 A. Wijerathne, A. Sawyer, R. Daya and C. Paolucci, Competition between Mononuclear and Binuclear Copper Sites across Different Zeolite Topologies, *JACS Au*, 2024, **4**(1), 197–215, DOI: 10.1021/jacsau.3c00632.

44 W. Huang, A. C. Johnston-Peck, T. Wolter, W.-C. D. Yang, L. Xu, J. Oh, B. A. Reeves, C. Zhou, M. E. Holtz, A. A. Herzing, A. M. Lindenberg, M. Mavrikakis and M. Cargnello, Steam-created grain boundaries for methane C–H activation in palladium catalysts, *Science*, 2021, **373**(6562), 1518–1523, DOI: 10.1126/science.abj5291.

45 J. J. Willis, E. D. Goodman, L. Wu, A. R. Riscoe, P. Martins, C. J. Tassone and M. Cargnello, Systematic Identification of Promoters for Methane Oxidation Catalysts Using Size- and Composition-Controlled Pd-Based Bimetallic Nanocrystals, *J. Am. Chem. Soc.*, 2017, **139**(34), 11989–11997, DOI: 10.1021/jacs.7b06260.

46 E. D. Goodman, A. S. Asundi, A. S. Hoffman, K. C. Bustillo, J. F. Stebbins, S. R. Bare, S. F. Bent and M. Cargnello, Monolayer Support Control and Precise Colloidal Nanocrystals Demonstrate Metal–Support Interactions in Heterogeneous Catalysts, *Adv. Mater.*, 2021, **33**(44), 2104533, DOI: 10.1002/adma.202104533.

47 J. W. A. Fischer, A. Brenig, D. Klose, J. A. van Bokhoven, V. L. Sushkevich and G. Jeschke, Methane Oxidation over Cu2+/[CuOH]+ Pairs and Site-Specific Kinetics in Copper Mordenite Revealed by Operando Electron Paramagnetic Resonance and UV/Visible Spectroscopy, *Angew. Chem., Int. Ed.*, 2023, **62**(34), e202303574, DOI: 10.1002/anie.202303574.

48 M. Tatlier, G. Munz and S. K. Henninger, Relation of Water Adsorption Capacities of Zeolites with Their Structural Properties, *Microporous Mesoporous Mater.*, 2018, **264**, 70–75, DOI: 10.1016/j.micromeso.2017.12.031.

49 P. Hurtado, Development of a Kinetic Model for the Oxidation of Methane over Pd/Al2O3 at Dry and Wet Conditions, *Appl. Catal., B*, 2004, **51**(4), 229–238, DOI: 10.1016/j.apcatb.2004.03.006.

50 P. Losch, W. Huang, O. Vozniuk, E. D. Goodman, W. Schmidt and M. Cargnello, Modular Pd/Zeolite Composites Demonstrating the Key Role of Support Hydrophobic/Hydrophilic Character in Methane Catalytic Combustion, *ACS Catal.*, 2019, **9**(6), 4742–4753, DOI: 10.1021/acscatal.9b00596.

51 H. Li, C. Paolucci, I. Khurana, L. N. Wilcox, F. Göltl, J. D. Albarracin-Caballero, A. J. Shih, F. H. Ribeiro, R. Gounder and W. F. Schneider, Consequences of Exchange-Site Heterogeneity and Dynamics on the UV-Visible Spectrum of Cu-Exchanged SSZ-13, *Chem. Sci.*, 2019, **10**(8), 2373–2384, DOI: 10.1039/C8SC05056B.

52 M. L. Bols, J. Ma, F. Rammal, D. Plessers, X. Wu, S. Navarro-Jaén, A. J. Heyer, B. F. Sels, E. I. Solomon and R. A. Schoonheydt, In Situ UV–Vis–NIR Absorption Spectroscopy and Catalysis, *Chem. Rev.*, 2024, **124**(5), 2352–2418, DOI: 10.1021/acs.chemrev.3c00602.

53 K. Narsimhan, K. Iyoki, K. Dinh and Y. Román-Leshkov, Catalytic Oxidation of Methane into Methanol over Copper-Exchanged Zeolites with Oxygen at Low Temperature, *ACS Cent. Sci.*, 2016, **2**(6), 424–429, DOI: 10.1021/acscentsci.6b00139.

54 R. Daya, M.-Y. Kim, L. Wei, U. Menon, H. An and C. Paolucci, Influence of Temperature, Water, and Dioxygen on the Interconversion of Monomeric and Dimeric Cu Configurations in Cu-SSZ-13, *ACS Catal.*, 2025, **15**(15), 13630–13644, DOI: 10.1021/acscatal.5c02958.

55 P. J. Smeets, B. F. Sels, R. M. van Teeffelen, H. Leeman, E. J. M. Hensen and R. A. Schoonheydt, The Catalytic Performance of Cu-Containing Zeolites in N2O Decomposition and the Influence of O2, NO and H2O on Recombination of Oxygen, *J. Catal.*, 2008, **256**(2), 183–191, DOI: 10.1016/j.jcat.2008.03.008.

56 S. Yashnik and Z. Ismagilov, Cu-Substituted ZSM-5 Catalyst: Controlling of DeNO*x* Reactivity via Ion-Exchange Mode with Copper–Ammonia Solution, *Appl. Catal., B*, 2015, **170–171**, 241–254, DOI: 10.1016/j.apcatb.2015.01.021.

57 A. A. Alswat, M. B. Ahmad, M. Z. Hussein, N. A. Ibrahim and T. A. Saleh, Copper Oxide Nanoparticles-Loaded Zeolite and Its Characteristics and Antibacterial Activities, *J. Mater. Sci. Technol.*, 2017, **33**(8), 889–896, DOI: 10.1016/j.jmst.2017.03.015.

58 J. M. Hayes, Practice and principles of isotopic measurements in organic geochemistry, in *Organic Geochemistry of Contemporaneous and Ancient Sediments*, ed. W. G. Meinschein, Great Lakes Section, Society of Economic Paleontologists and Mineralogists, Bloomington, Indiana, 1983, pp. 5-1–5-31.

59 K. Narsimhan, K. Iyoki, K. Dinh and Y. Román-Leshkov, Catalytic Oxidation of Methane into Methanol over Copper-Exchanged Zeolites with Oxygen at Low Temperature, *ACS Cent. Sci.*, 2016, **2**(6), 424–429, DOI: 10.1021/acscentsci.6b00139.